ELSEVIER

International Journal of Heat and Fluid Flow 22 (2001) 500–508

International Journal of HEAT AND FLUID FLOW

www.elsevier.com/locate/ijhff

Large-eddy simulation of flow and heat transfer in an impinging slot jet

T. Cziesla [a], G. Biswas [b,*], H. Chattopadhyay [c], N.K. Mitra [a]

[a] *Institut für Thermo- und Fluiddynamik, Ruhr Universität Bochum, 44721 Bochum, Germany*
[b] *Department of Mechanical Engineering, Indian Institute of Technology, Kanpur 208 016, India*
[c] *Central Mechanical Engineering Research Institute, Durgapur 713 209, India*

Received 15 October 1999; accepted 26 January 2001

Abstract

The flow field due to an impinging jet at a moderately high Reynolds number, emanating from a rectangular slot nozzle has been computed using a large eddy simulation (LES) technique. A dynamic subgrid-scale stress model has been used for the small scales of turbulence. Quite a few successful applications of the dynamic subgrid-scale stress model use planar averaging to avoid ill conditioning of the model coefficient. However, a novel localization procedure has been attempted herein to find out the spatially varying model coefficient of the flow. The flow field is characterized by entrainment at the boundaries. Periodic boundary conditions could not be used on all the boundaries. The results reveal the nuances of the vortical structures that are characteristic of jet flows. The stress budget also captures a locally negative turbulence production rate. The calibration of the model has been made through prediction of the normalized axial velocity profile and heat transfer on the impingement plate. The computed results compare favorably with the experimental observations, especially in the stagnation zone.

Keywords: Impinging jet; Turbulence; Heat transfer; Large-eddy simulation

1. Introduction

Impinging jets are used for several industrial applications. Jet impingement is a common concern for the aerodynamicists dealing with VSTOL aircrafts. The ground impingement of single or multiple jets and the influence of upwash fountains on ground-based structures during the take-off operation are challenging topics of research. Impinging jets are also used for heating, cooling and drying of impingement surfaces. The jets emanate from the nozzles as laminar, but the evolution of instability and the eventual transition to turbulence take place a little distance in the downstream of the orifice (Becker and Massaro, 1968). For a round jet, a stagnation point is formed at the center on the impingement surface (Gutmark et al., 1978). The flow develops along the impingement surface in the form of a wall jet. In the stagnation zone, the strong acceleration keeps the boundary layer laminar (Martin, 1977). A second transition is usually brought about immediately after the jet is transformed near the wall into a decelerated wall jet. The heat or mass transfer rate at the stagnation point is very high. Away from the stagnation point, a rapid variation of heat transfer is observed. In the case of a second transition, another peak in transport rate is attained (Martin, 1977). Gardon and Akfirat (1965) observed that the level of turbulence in the jet had a strong influence on the rate of heat transfer from the impingement plate. They deployed slot jets impinging on a flat plate. Donaldson et al. (1971) used a round jet and found that the heat transfer characteristics, away from the stagnation point, are similar to a normal turbulent boundary layer in an external flow having a free-stream velocity equal to the local maximum velocity in the wall jet. Experimental investigations of heat transfer by jets on impingement surfaces have been summarized by Viskanta (1993).

The strongest indication of a coherent structure in the self-preserving region of a plane jet is the flapping of a jet in still air. The presence of such large-scale organized structures (Mumford, 1982) in a plane jet has been established by Antonia et al. (1983). It is possibly worth mentioning that the local flapping can be eliminated (Bradbury, 1965) by a moving external stream. In another study, Antonia et al. (1986) showed an intimate connection between the double-roller eddies of a plane jet and the span-wise eddies of a Karman vortex street. They also found that the contributions by the coherent and random motions to the averaged momentum and thermal energy transport are generally of the same order of magnitude.

Craft et al. (1993) have reported numerical simulations of turbulent impinging jets. The authors evaluated various turbulence models for predicting the heat transfer in the stagnation region. None of the models was able to yield satisfactory

* Corresponding author. Tel.: +91-512-597656; fax: +91-512-590260.
E-mail address: gtm@iitk.ac.in (G. Biswas).

0142-727X/01/$ - see front matter
PII: S0142-727X(01)00105-9

Notation

B	slot nozzle width
C	model parameter of eddy viscosity model, Eq. (15)
conv	convective terms of Navier–Stokes equations, Eq. (7)
diff	diffusive terms of Navier–Stokes equations, Eq. (7)
H	height of the computational domain
h	nozzle-to-plate spacing, non-dimensionalized with B
k	turbulent kinetic energy
L	nozzle length
Nu	Nusselt number, given by Eq. (38)
p	pressure
P	production rate of turbulence
Pr	Prandtl number of the fluid
q	heat flux between impingement plate and fluid
Re	Reynolds number
S	hydraulic diameter ($2B$)
T	temperature
t	time
u	velocity component in x-direction
v	velocity component in y-direction
w	velocity component in z-direction
w_{in}	nozzle exit velocity
W	width of the computational domain
x, y, z	spatial coordinates

Greeks

ν	kinetic viscosity
τ	turbulent shear stress
Θ	non-dimensional temperature, T/T_{in}

Subscripts

∞	ambience
av	average
B	slot width
in	inflow plane
max	maximum
w	wall

Superscripts

$*$	intermediate level
n	current time-step
$'$	subgrid scale component
$''$	fluctuating component

results in the stagnation zone. The eddy viscosity model achieved very poor agreement with the experiments because of the basic weakness of the eddy viscosity stress–strain relation. Three other models were of the second moment closure type. Two of them failed due to the incorrect response of its submodel of the wall-reflection process in a stagnating strain field. The third model worked reasonably well but needed a refinement in the sublayer region through a low-Reynolds number second moment closure. Leschziner and Ince (1994) and Suga (1995) have performed numerical simulation of turbulent impinging jets by making use of Reynolds stress transport models and nonlinear k–ε models, respectively.Both the investigations show marked improvements in flow predictions compared to the standard k–ε predictions. The nonlinear k–ε model predicts heat transfer in satisfactory agreement with the experimental results of Baughn and Shimizu (1989).

The flow field of an impinging jet is quite complex. However, direct numerical simulation (DNS) is the proper approach to analyze such complex flows.In order to resolve all scales of motion by the DNS approach the number of grid points needed is order of $Re^{9/4}$. Large eddy simulation (LES) is a technique intermediate between the direct simulation of turbulent flows and the solution of the Reynolds-averaged equations through closure approximations. In LES, the contribution of the large-scale structures to momentum and energy transfer is computed directly and the effect of the smallest scales of turbulence is modeled. Since the small scales are more homogeneous and universal and less affected by the boundary conditions than the large eddies, the modeling here is generally more acceptable. However, while it still requires reasonably fine meshes, it can be used at much higher Reynolds number than DNS. If the small scales obey inertial range dynamics, the cost of computation is independent of Reynolds number (Piomelli, 1994).

Laschefski et al. (1994, 1996, 1997) have presented flow and temperature fields of laminar impinging jets. In their investigations, the nozzle height from the impingement surface and Reynolds numbers were varied. It has been found that for a given geometry (e. g. distance of the nozzle from the surface is $2B$, where B is the slot width), the flow field changes from steady laminar to unsteady periodic at $Re_{2B} > 400$ and to aperiodic at $Re_{2B} > 600$ (Laschefski et al., 1994).

Gao and Voke (1995) have presented the results of LES of thermally inhomogeneous jets issuing into an enclosed pool and impinging on a plate. Voke and Gao (1998) have further extended the investigation and shown that the mean temperature distribution in the jet serves to concentrate cold fluid near the boundaries and hot fluid near the centre, leading to a hot jet impingement on the plate and cold fluid in the recirculating regions. A closer observation reveals the strong attenuation of the thermal eddies as they move towards the plate.

The purpose of the present work is to perform LES of the flow field of axial jets emanating from a rectangular slot nozzle and impinging on a heated flat surface. The results are expected to reveal the detailed flow structure, form a basis of understanding the flow phenomena and predict the heat transfer accurately at the stagnation point.

2. Basic equations and method of solution

Fig. 1 shows the geometry of interest. It consists of a semi-enclosed rectangular slot jet of width B and length L_y. The impingement plate is of length L_x and the distance between the impingement plate and the top wall is $h = L_z$.

All velocity variables are non-dimensionalized by w_{in} and the length dimensions are non-dimensionalized by the slot width B. If the Navier–Stokes equations are approximated by a finite difference (or finite volume) scheme, then an approximation filter (top hat filter) is introduced which filters out all subgrid-scales with scales smaller than $\overline{\Delta}$, where $\overline{\Delta}$ is the filter size. In the finite difference procedure (Schumann, 1975)

$$\overline{\Delta} \equiv \left(\overline{\Delta}_1 \overline{\Delta}_2 \overline{\Delta}_3\right)^{1/3}, \tag{1}$$

where $\overline{\Delta}_i$ is the grid size in x, y- and z-direction.

If the filtering operation is applied to the governing equations, the filtered Navier–Stokes and continuity equations for an incompressible flow assume the form

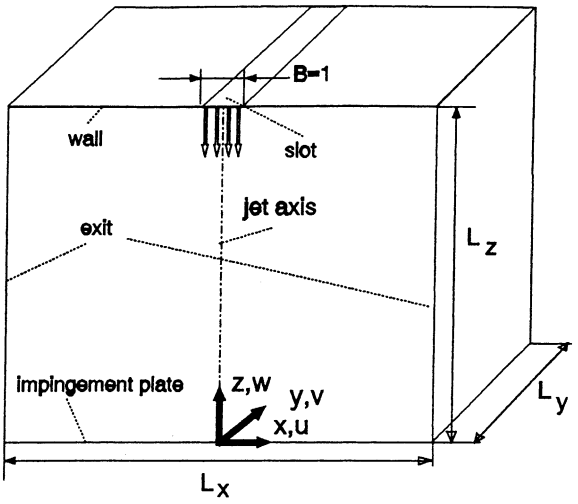

Fig. 1. Imping slot jet, geometry and coordinates system.

$$\frac{\partial \overline{u}_i}{\partial x_i} = 0, \tag{2}$$

$$\frac{\partial \overline{u}_i}{\partial t} + \frac{\partial(\overline{u_i u_j})}{\partial x_j} = -\frac{\partial \overline{p}}{\partial x_i} + \frac{1}{Re_B}\frac{\partial^2 \overline{u}}{\partial x_j^2} - \frac{\partial \tau_{ij}}{\partial x_j}, \tag{3}$$

where the index $i = 1, 2, 3$ refers to the x-, y- and z-directions, respectively, and repeated indices imply summation. The Reynolds number is defined as $Re_B = w_{\text{in}}B/\nu$. The term τ_{ij} defines the subgrid scale stresses, which may be written as

$$\tau_{ij} = \left(\overline{\overline{u}_i u'_j} + \overline{u'_i \overline{u}_j} + \overline{u'_i u'_j}\right). \tag{4}$$

The overbar represents the filter operator and prime denotes subgrid scale components. The subgrid scale stresses are computed using a dynamic subgrid-scale model.In the present simulation, we have used top hat filters in the spatial directions consistent with the use of finite differences (finite volume discretization) in these directions. With the choice of such filters, it can be shown that the difference $(\overline{u_i u_j}) - \overline{u}_i \overline{u}_j$ is of second order in the filter width which is the same as the truncation error in the second-order differencing method used in this analysis. Thus replacing $(\overline{u_i u_j})$ by $\overline{u}_i \overline{u}_j$, the momentum equation (3) may be rewritten as

$$\frac{\partial \overline{u}_i}{\partial t} + \frac{\partial}{\partial x_j}\left(\overline{u}_i \overline{u}_j\right) = -\frac{\partial \overline{p}}{\partial x_i} + \frac{1}{Re_B}\frac{\partial^2 \overline{u}_i}{\partial x_j^2} - \frac{\partial}{\partial x_j}\tau_{ij}. \tag{5}$$

The energy equation for incompressible flows may be correspondingly written as

$$\frac{\partial \overline{\Theta}}{\partial t} + \frac{\partial(\overline{u}_j \overline{\Theta})}{\partial x_j} = \frac{1}{Re_B Pr}\nabla^2 \overline{\Theta} - \frac{\partial q_j}{\partial x_j}, \tag{6}$$

where $\overline{\Theta}$ is the resolved-scale temperature (non-dimensionalzied), q_j is the subgrid scale heat transfer and will be defined later in an analogous way to τ_{ij}. Air has been assumed as the working fluid hence the Prandtl number, Pr of the fluid in this simulation has been taken as 0.7.

A fractional-step finite-difference method due to Kim and Moin (1985) has been used to solve the set of equations (2) and (5) on a staggered grid arrangement (Harlow and Welch, 1965). The discretization scheme is second order in space (central differences). The important factors in the choice of the spatial differencing strategy are the formal order of accuracy and the global conservation properties of the numerical scheme. The order of accuracy relates the accuracy of the solution whereas the conservative property improves the stability of the scheme, and the physical realism of the predicted fields. Temporal and spatial accuracy are extremely important in LES. The numerical scheme must be second order on a staggered grid and fourth order on a collocated grid. Mittal and Moin (1997) have recently shown that the second-order central differencing with staggered grid provides the energy spectra that is in excellent agreement with its experimental counterpart. In another recent study, turbulent boundary layer separating at a backstep has been investigated by Le et al. (1997) with a second-order central difference scheme on staggered grids. The simulation provides excellent match with the concurrent experimental data. For the convective terms the Adams–Bashforth method is used in order to ensure second-order accuracy in time. The viscous terms are discretized by the Crank–Nicholson scheme. A two-step time advancement scheme starts with the calculation of an intermediate velocity field, u_i^* as

$$\frac{\overline{u}_1^* - \overline{u}_i^n}{\Delta t} = -\frac{3}{2}\text{conv}^n + \frac{1}{2}\text{conv}^{n-1} + \frac{1}{2Re_B}\left(\text{diff}^n + \text{diff}^{n+1}\right), \tag{7}$$

where the convective and diffusive terms are denoted by conv and diff. The index n symbolizes the current time-step, $(n-1)$ stands for the previous time-step and * signifies the intermediate step. The velocities for the next time-step $(n+1)$ are related to the intermediate values through

$$u_i^* = \overline{u}_i^{n+1} + \Delta t \nabla \overline{p}^{n+1}. \tag{8}$$

Invoking the continuity equation (2) in Eq. (8) one obtains the following Poisson equation for the pressure field:

$$\nabla^2 \overline{p}^{n+1} = \frac{1}{\Delta t}\nabla \cdot \overline{u}_i^*. \tag{9}$$

Once Eq. (9) is solved, the intermediate velocity field u_i^* is corrected to yield the velocity field for the next time-step in the following way:

$$\overline{u}_i^{n+1} = \overline{u}_i^* - \Delta t \nabla \overline{p}^{n+1}. \tag{10}$$

The energy equation (6) can be treated in the same way as the momentum equations (Grötzbach, 1986) and, from the resolved scale temperature fields at different time levels, the time-averaged temperature field is finally obtained.

2.1. Subgrid-scale closure

The terms τ_{ij} and q_j in Eqs. (5) and (6) are the contribution of small scales to the large-scale transport equation. In the volume averaging approach of Schumann (1975), $\overline{u_i}$ is constant within each control volume and $\overline{u'_i} = 0$. Finally, Eq. (4) will assume the form

$$\tau_{ij} = \overline{u'_i u'_j} \tag{11a}$$

and in a similar way

$$q_j = \overline{u'_j \Theta'} \tag{11b}$$

as mentioned earlier, the overbar represents the filter operator. These stresses are similar to the classical Reynolds stresses that result from time- or ensemble-averaging of the advection fluxes, but differ in that they are consequences of spatial averaging and go to zero if the filter width $\overline{\Delta}$ goes to zero.

The most commonly used subgrid scale model of Smagorinski (1963) is based on the gradient transport hypothesis, which correlates τ_{ij} to large-scale strain-rate tensor

$$\tau_{ij} = -2\nu_T \overline{S}_{ij} + \frac{\delta_{ij}}{3}\tau_{kk}, \tag{12a}$$

and in a similar manner

$$q_j = -\frac{2}{Pr_t} v_T \frac{\partial \overline{\Theta}}{\partial x_i}, \tag{12b}$$

where v_T is the eddy viscosity, δ_{ij} is the Kronecker delta, Pr_t is the turbulent Prandtl number, $\tau_{kk} = \overline{u_k' u_k'}$ and $\overline{S}_{ij}$ is given by

$$\overline{S}_{ij} = \frac{1}{2}\left(\frac{\partial \overline{u}_i}{\partial x_j} + \frac{\partial \overline{u}_j}{\partial x_i}\right). \tag{13}$$

Lilly (1967) proposed the following formula to obtain the eddy viscosity:

$$v_T = \left(C_S \overline{\Delta}\right)^2 |\overline{S}|. \tag{14}$$

Here C_S is a constant, $\overline{\Delta}$ is the grid filter scale and $|\overline{S}| = \left(2\overline{S}_{ij}\overline{S}_{ij}\right)^{1/2}$. Substitution of (14) in (12a) yields

$$\tau_{ij} - \frac{\delta_{ij}}{3}\tau_{kk} = 2C\overline{\Delta}^2 |\overline{S}| S_{ij} = -2C\beta_{ij}. \tag{15}$$

The quantity C is the Smagorinsky coefficient and it depends on the type of flow under consideration (Canuto and Cheng, 1997). Germano et al. (1991) and Lilly (1992) suggested a method to calculate C, for each time-step and grid-point, dynamically from field data. In addition to the grid filter (denoted by an overbar), which signifies the resolved and subgrid scales, a test filter (denoted by a caret over the overbar) is used. The width of the test filter is larger than the grid filter width. The test filter defines a new set of stresses: the test-level subgrid-scale stresses or subtest-scale stresses, T_{ij} given by

$$T_{ij} = -\widehat{\overline{u_i}\overline{u_j}} - \hat{\overline{u}}_i \hat{\overline{u}}_j. \tag{16}$$

Eq. (16) can also be expressed in terms of the Smagorinsky closure as

$$T_{ij} - \frac{\delta_{ij}}{3} T_{kk} = -2C\hat{\Delta}^2 |\hat{\overline{S}}| \hat{\overline{S}}_{ij} = -2C\alpha_{ij}, \tag{17}$$

where

$$\hat{\overline{S}}_{ij} = \frac{1}{2}\left(\frac{\partial \hat{\overline{u}}_i}{\partial x_j} + \frac{\partial \hat{\overline{u}}_j}{\partial x_i}\right) \tag{18}$$

and

$$\hat{\Delta} = \left(\hat{\Delta}_1 \hat{\Delta}_2 \hat{\Delta}_3\right)^{1/3}, \quad \hat{\Delta}/\overline{\Delta} = 2. \tag{19}$$

The major contribution to the subgrid-scale model brought about by Germano et al. (1991) is the identification that consistency between (15) and (17) depends on a proper choice of C. This is achieved by subtraction of the test-scale average of τ_{ij} from T_{ij}, (see Lilly, 1992; Hoffmann and Benocci, 1994; Najjar and Tafti, 1996) to obtain

$$L_{ij} = \ell_{ij} - \frac{\delta}{3}\ell_{kk} = T_{ij} - \hat{\tau}_{ij} = -2C\alpha_{ij} + 2\widehat{C\beta_{ij}} \tag{20}$$

with

$$\beta_{ij} = \overline{\Delta}^2 |\overline{S}| \overline{S}_{ij}, \tag{21}$$

$$\alpha_{ij} = \hat{\Delta}^2 |\hat{S}| \hat{S}_{ij}. \tag{22}$$

Eqs. (15), (17), (20), (21) and (22) are five independent equations which cannot be solved for the model constant C because it appears in a filter operation (Eq. (20)). Lilly (1992) and Zang et al. (1993) have suggested the following assumption:

$$\widehat{C\beta_{ij}} = C\hat{\beta}_{ij}, \tag{23}$$

which enables Eq. (20) to be written in the form

$$E_{ij} = L_{ij} + 2C\alpha_{ij} - 2C\hat{\beta}_{ij}. \tag{24}$$

E_{ij} is the residue of Eq. (24). Application of the least-squares technique to minimize the residual gives the following expression for C:

$$C = -\frac{1}{2}\frac{\langle L_{ij}(\alpha_{ij} - \hat{\beta}_{ij})\rangle}{\langle (\alpha_{mn} - \beta_{mn})(\alpha_{mn} - \hat{\beta}_{mn})\rangle}, \tag{25}$$

where

$$L_{ij} = \widehat{\overline{u}_i \overline{u}_j} - \hat{\overline{u}}_i \hat{\overline{u}}_j \tag{26}$$

and $\langle\ \rangle$ means an average over a plane in the model for which the flow is homogeneous. The least-square minimization technique has been used by Piomelli (1994) to compute the flow in a plane channel at Reynolds numbers between 200 and 2000. A limitation of the dynamic model is the plane averaging mentioned earlier. For an essentially three-dimensional flow like the rectangular impinging jet, we propose to use a local averaging over the test filter cell. Zang et al. (1993) performed this local averaging and also constrained the effective viscosity (molecular and eddy viscosity) to be non-negative for recirculating flows.

In addition to the above-mentioned local averaging, we perform a modification of Eq. (23) as suggested by Piomelli and Liu (1995). Mathematically, Eq. (23) is inconsistent because C ceases to be a function of space (Piomelli and Liu, 1995). Ghosal et al. (1995) have developed a consistent procedure without making use of the least-square approach. It is necessary to obtain the solution of an integral equation for calculating C by this procedure. The computational effort associated with the iterative solution is significantly high. Piomelli and Liu (1995) have suggested a simpler approach based on modification of Eq. (20) as

$$-2C\alpha_{ij} = L_{ij} - 2\widehat{C^*\beta_{ij}}. \tag{27}$$

On the right-hand side an estimate of the coefficient C is substituted by C^*. The value of C^* is assumed to be known. In the event, minimization of the sum of the squares results in

$$C(x,y,z) = -\frac{1}{2}\frac{(L_{ij} - 2\widehat{C^*\beta_{ij}})\alpha_{ij}}{\alpha_{mn}\alpha_{mn}}. \tag{28}$$

This is the equation used here for calculating the model coefficient C. There are various ways to obtain C^* at time-step n. Piomelli and Liu (1995) indicated that there is no significant difference between zeroth- and first-order approximations for estimating C^*. The present computation uses a zeroth-order approximation through the value at the previous time-step.

$$C^* = C^{n-1}. \tag{29}$$

Even though we have used the local averaging procedure of Zang et al. (1993) spurious values of C appeared during the calculation. After averaging, the following additional constraint was imposed on the averaged C:

$$C \geqslant 0. \tag{30}$$

This restriction is necessary to avoid negative viscosity (Ghosal et al., 1995). Thus, once v_t is known, τ_{ij} and q_j can be computed from Eqs. (12a) and (12b).

2.2. Boundary conditions

At the exit of the jet, a constant velocity profile and, at the fixed walls, no-slip conditions are assumed. At the lower (impingement) plate, the no-slip condition is implemented for the diffusive terms by direct calculation of the near wall flow using a locally fine grid. A linear velocity profile for the wall gradients is assumed (similar to laminar calculations). Therefore the distance between the center of the near wall grid cells and the

impingement plate ($z_p^+ = z_p Re_\tau$) is smaller than 1. The parameter Re_τ is the Reynolds number based on friction velocity u_τ. At the upper wall, the logarithmic velocity profile (Cziesla et al., 1996) for calculation of the averaged (denoted by $\langle\ \rangle$) wall shear stress distribution has been used. The approach described in Schumann (1975) sets

$$\frac{\tau_w}{U_p} = \frac{\langle \tau_w \rangle}{\langle U_p \rangle} \tag{31}$$

for the instantaneous wall shear stress τ_w. The resultant velocity at the near wall cell is U_p. Periodic boundary conditions are used at $y = 0$ and $y = 2$. The exit planes ($x = -5$ and $x = 5$) have inflow from the local ambient due to entrainment effect (Laschefski et al., 1994); the exit boundary conditions have to be derived. Integration of Eq. (9) gives

$$\int\int_G \int (\nabla^2 \overline{p}^{n+1})\,\mathrm{d}\forall = \frac{1}{\Delta t}\int\int_G \int (\nabla . \overline{u}^*)\,\mathrm{d}\forall. \tag{32}$$

Application of the Gauss divergence theorem leads to

$$\int_\partial \int_G \left(\frac{\partial \overline{p}^{n+1}}{\partial n}\right)\mathrm{d}S = \frac{1}{\Delta t}\int\int_G \int (\nabla . \overline{u}^*)\,\mathrm{d}\forall. \tag{33}$$

It is easy to show that the commonly used pressure boundary condition, such as, zero first derivative, cannot be used for jet flows. Since the intermediate velocity field $\overline{u}_i^*$ is only the solution of momentum equations and does not fulfil the global continuity, the left-hand side of Eq. (33) cannot be equated to zero. Our investigation for laminar impinging jets produced good results with $p = p_\infty$, the ambient pressure at the exit (see Laschefski et al., 1994). For the present situation, we implemented a condition suggested by Childs and Nixon (1986) and Grinstein et al. (1987) so that pressure fluctuations across the exit plane are possible

$$\overline{p}_e = 0.7\overline{p}_i + 0.3\overline{p}_\infty. \tag{34}$$

The pressure at the exit plane, $\overline{p_e}$ is an interpolated value between the pressure of the last interior cell of the domain, $\overline{p_i}$ and the ambient pressure, which is known a priori.

Vanishing first derivative conditions for the tangential velocities are assumed at the exit. The normal velocity, as usual for the interior points on the exit plane is set to

$$\overline{u}_i^{n+1} = \overline{u}_1^* - \Delta t \nabla \overline{p}^{n+1}. \tag{35}$$

2.3. Computational domain and grid size

The width of the domain (see Fig. 1), L_y in the y-direction is 2. As such the extent of the y-dimension is assumed large and L_y is the dimension of a periodic element. It may be mentioned here that the dimensions of the large-scale structures in this direction have been found to be less than $L_y = 2$ (see Cziesla, 1998). The height of the computational domain, h has been varied between 8 and 12; the length, L_x is 10. A uniform velocity profile of $w_{in} = 1$ is deployed at the exit of the nozzle slot. Computations have been performed with a grid of $152 \times 22 \times 79 = 264176$ cells. In the implementation of LES the filter size is taken equal to the grid size. Therefore, increasing the resolution changes the problem by invoking new modes. Hence the usual concept of grid independence in the standard implementation of LES is absent (Ghosal, 1999). However, the Nusselt number being a derived parameter of final interest from the solution, a grid sensitivity test was performed by using grid meshes of $102 \times 18 \times 75$ and $182 \times 26 \times 81$. The average Nusselt number due to the present grid mesh differs from that of the extrapolated grid-insensitive situation by less than 2%. However, for the present grid, the size of Δx is 0.05 between $x = -0.05$ and $+0.5$. Outside this region, Δx has been increased continuously by 1%. In the y-direction, a uniform grid of $\Delta y = 0.1$ has been used. In the z-direction, $\Delta z = 0.00469$ has been used on the impingement plate and then Δz has been increased in the normal direction continuously by a factor of 1.14. For time-averaging, 260 instantaneous fields over 25 000 time-steps have been used. The computations have been performed on an IBM RISC 6000-58 H dedicated Workstation.

3. Results and discussion

3.1. Flow field predictions

Fig. 2 shows instantaneous velocity vectors for a Reynolds number of 5800 at the $y = 1$ plane. The jet shows a laminar structure at the exit and the laminar regime continues for a short distance downstream. At $z = 6$ the unstable laminar shear layers begin to break down to vortices. In the figure, the letters L (for the left side) and R (for the right side) have denoted these vortices and the motion of the individual vortices has been examined as they move along the surface and out of the domain of interest. The flow shows a somewhat steady character near the impingement point. After the impingement, the jet forms into two wall jets on the surface. Entrainment from the upper part of the domain is induced by vortices wrapping the ambient fluid about themselves.

Gutmark and Wygnanski (1976) indicate that the mean axial velocity on the jet-axis decays linearly with axial distance. In the present study, the distribution of the normalized jet axial velocity w/w_m along x/b_w at different distances, (z) from the impingement plate has been analyzed. Fig. 3(a) shows the self-similar development of the axial velocity between $z = 12$ and $z = 4$. The present computation compares reasonably well with the experimentally obtained Gaussian-like curve of Namer and Ötügen (1988). The comparison supports the predictive accuracy of the simulation. The temperature field depends strongly upon the accuracy of the velocity field, and thus it is essential that the velocity field for the present computations should compare favorably with experiments. The small discrepancy at larger x ($x = 0$ being the jet axis) can be attributed to the difference in local ambient conditions between the experiment and the numerical simulation. For this partic-

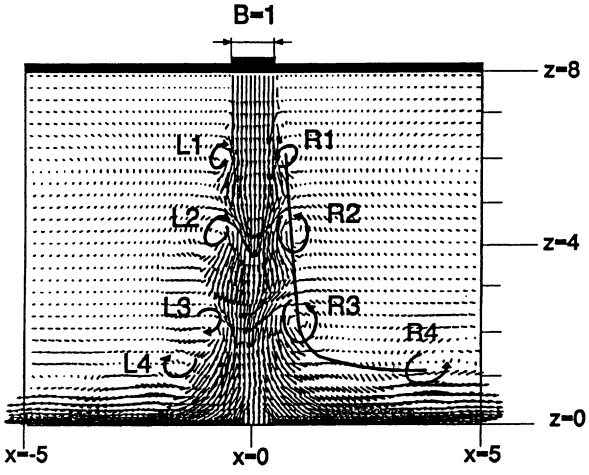

Fig. 2. Instantaneous velocity vectors on x–z plane, $Re_B = 5800$.

ular case, the axial velocity was averaged over the width of the domain of interest to obtain a two-dimensional field. The height of the computation domain was taken as $z = 20$ and the Reynolds number was $Re_B = 10000$. The variable, b_w is the half-width of the jet, the distance from the jet axis to the point where the axial velocity has fallen to half its centerline value. Fig. 3(b) shows the distribution of the root-mean-square value of the normal component of velocity. As in Fig 3(a), the velocity component was averaged over the width of the domain of interest for this case as well. Solid squares and triangles indicate the values corresponding to present investigation. Up to a distance of $\xi = 4$, there is a good match between the predicted values due to present computation and the values obtained by other researchers. However, for a Reynolds number of 10000, beyond a distance of $\xi = 4$, present predictions deviate from the predictions of Hoffmann and Benocci (1994). It is interesting to note that beyond $\xi = 8$, again there is a good match between the present prediction and the prediction of Hoffmann and Benocci (1994). The predicted values due to present computation, for a Reynolds number of 2000, matched quite well with those of experimental values of Namer and Ötügen (1988).

Fig. 4 shows the variation of time-averaged value of the normal velocity component, $\langle w_m \rangle$ and the fluctuating quantity, $\langle w'' \rangle$ along z at $x = 0$ and $y = 0$. It is to be noted that w' is the subgrid scale component while w'' is the fluctuating component. The Reynolds number for this case is 5800 and $z = 8$. It is readily seen that $\langle w_m \rangle$ remains essentially constant (equal to

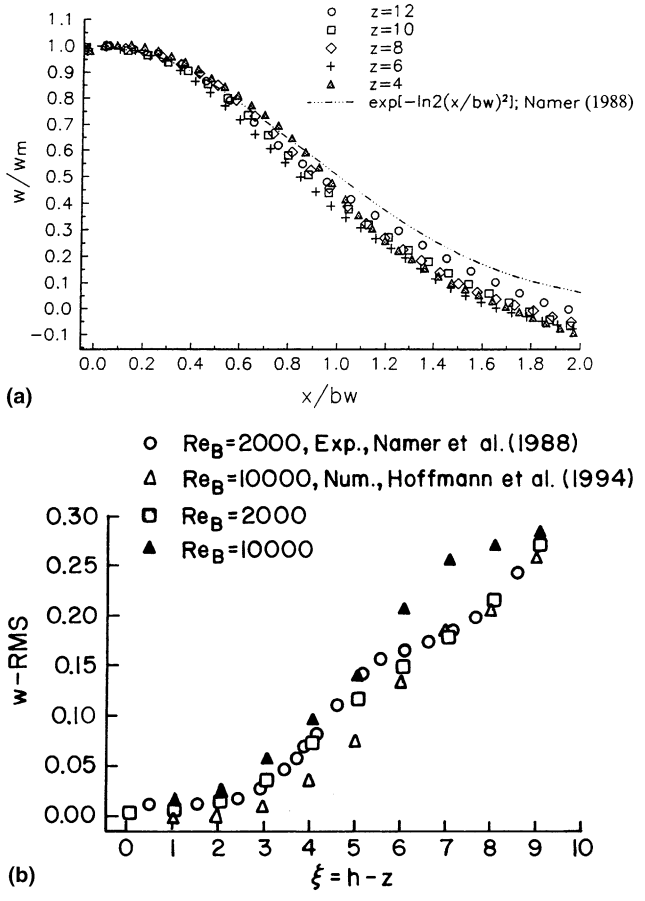

Fig. 3. (a) Normalized axial velocity distribution of the jet, $Re_B = 10000$. (b) Distribution of the root-mean-square value of the normal component of velocity.

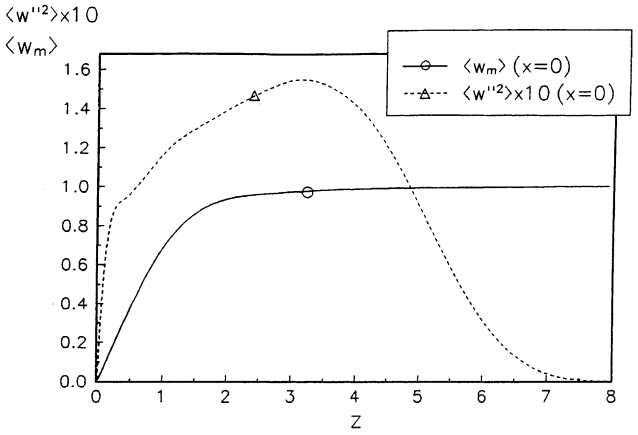

Fig. 4. The decay of time-mean centerline axial velocity and normal-stress, $Re_B = 5800$.

$\overline{w}_{in} = 1$) down to $z = 3.5$. The decay of $\langle w_m \rangle$ is most pronounced between $z = 1$ and $z = 0$. This is in conformity with the experimental investigation of Gardon and Akfirat (1965), where they observed that the reduction in impingement velocity started at the distance of a slot-width away from the plate. The turbulent normal stress $\langle w''^2 \rangle$ is essentially zero until one slot width downstream of the jet exit. Thereafter it increases sharply to the maximal at $z = 3.5$. From a distance of $0.3B$ away from the impinging plate, it falls down rapidly to zero at the stagnation point. On the scales of the figure, we do not see the variation close to the wall; in fact all the turbulent quantities vanish at the wall.

A measure of the level of fluctuation is taken to be the root-mean-square of the fluctuating quantity. The distribution of turbulent normal stress, $\langle w''^2 \rangle$ in the wall normal direction has been presented in Fig. 5. At $x = 0.5$ (close to the jet centerline) the values of $\langle w''^2 \rangle$ near $z = 2.0$ is 0.022 and then the quantity gradually approaches zero on the impingement plate ($z = 0$). At $x = 3$, we can observe a characteristic feature of wall flows. For this particular x location, the maximum value of the normal stress $\langle w''^2 \rangle$, 0.015, occurs at $z = 0.9$. The turbulent kinetic energy production rate is the quantity given by

$$P = -\left\{ \langle u_i'' u_j'' \rangle \frac{\partial \langle u_i \rangle}{\partial x_j} \right\}. \tag{36}$$

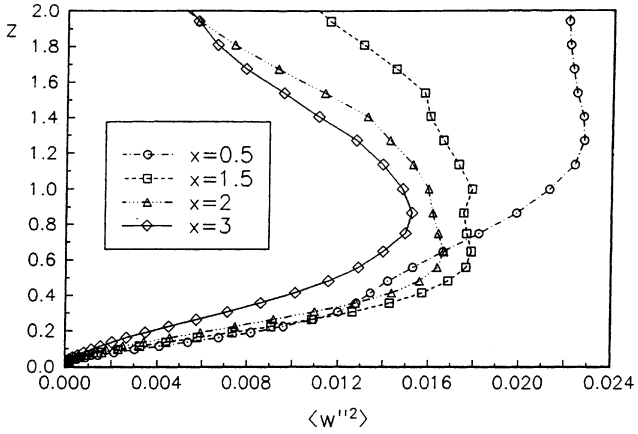

Fig. 5. Distribution of turbulent normal stress near the impinging plate, component perpendicular to the plate, $Re_B = 5800$.

Fig. 6(a) shows the distribution of the energy production rate P in the wall-jet region. The production rate of turbulence, P sustains the turbulence in the budget equation. Fig. 6(b) shows the same quantity closer to the wall. Fig. 6(a) indicates that at a large distance away from the impingement plate the production rate is high only for $x = 1$. At a larger distance from the jet axis ($x > 1$) the turbulence production rate is marginal for $z > 2$. For $x > 1$, the region very close to the impingement plate is influenced by intense interaction between the jet and the local ambience. The peak values of P at different distances away from the jet axis are observed to lie in the region $0.5 < z < 1.5$. The mathematical expression of P makes it clear that the gradient of the mean velocities determines the production and this serves to exchange kinetic energy between the mean flow and the turbulence. This helps to explain the high values of P at the shear layer and close to the impingement plate (Fig. 6(b)). The term P, in its physical sense, drains kinetic energy from the mean flow in the large scales and produces turbulent energy in the smaller scales. When the term P becomes negative, the energy flow is in the reverse direction signifying the energy transfer from the turbulent field to the mean field. Fig. 6(b) shows that for each x there is a small region with negative production rate. The negative value becomes smaller as z increases.

The production term near the impingement point can be simplified by ignoring the contributions from shear stresses and using the continuity relation for a two-dimensional flow ($\partial\langle u\rangle/\partial x = -\partial\langle w\rangle/\partial z$) as

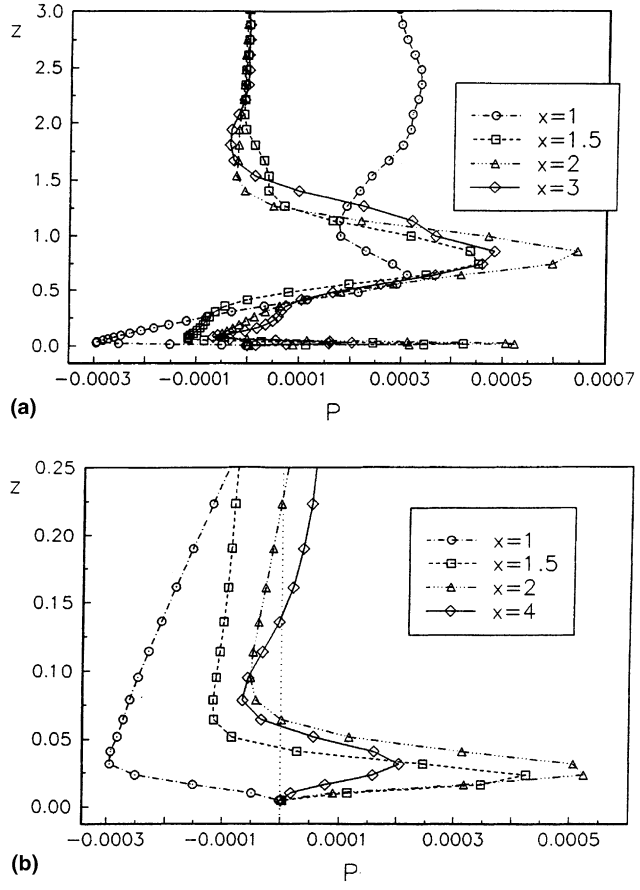

Fig. 6. (a) Distribution of production rate of turbulence near the impingement plate ($0 \leqslant z \leqslant 3.0$), $Re_B = 5800$. (b) Distribution of production rate of turbulence near the impingement plate ($0 \leqslant z \leqslant 0.25$), $Re_B = 5800$.

$$P = -\left\{ (\langle u''u''\rangle - \langle w''w''\rangle)\frac{\partial\langle u\rangle}{\partial x} \right\}. \tag{37}$$

The above expression signifies that the production rate of kinetic energy near the impingement point is proportional to the difference of turbulent normal stresses. The present computation shows (Fig. 7) that near the impingement point, i.e., for $x = 0.5$ and $x = 1.0$, $\partial\langle u\rangle/\partial x > 0$. Hence, the reason for negative production rate at $x = 1$, as shown by Fig. 6(b) can be attributed to the occurrence of $(\langle w''^2\rangle - \langle u''^2\rangle) > 0$ in the region of impingement point.

3.2. Prediction of heat transfer

The energy equation can be treated in the same way as the momentum equations (Grötzbach, 1986). Thus from the resolved-scale temperature fields, finally the time-average temperature field is obtained. The local Nusselt number on the impingement plate is defined as

$$Nu = \frac{\partial\langle\Theta\rangle/\partial z|_{\mathrm{w}}}{\overline{\Theta}_{\mathrm{w}} - \overline{\Theta}_{\mathrm{in}}}, \tag{38}$$

where $\overline{\Theta}_{\mathrm{w}}$ and $\overline{\Theta}_{\mathrm{in}}$ are the non-dimensional temperature of the impingement plate and the temperature of the fluid at the nozzle exit, respectively. The Nusselt number distribution is averaged over the spanwise (y)-direction to obtain the span-averaged Nu.

The heat transfer results have been compared with the experimental results of Sparrow and Wong (1975) and Schlünder et al. (1970). Fig. 8 compares the computational and experimental span-average Nusselt number distribution for $Re_B = 950$. The results show satisfactory agreement between the predicted value and the experiment.

Sparrow and Wong (1975) used a naphthalene sublimation technique to determine mass transfer rates. Following the analogy between heat and mass transfer, a correlation was used to predict the local Nusselt number from local Sherwood number

$$Nu = \left(\frac{Pr}{Sc}\right) Sh^r, \tag{39}$$

where r was set equal to 0.4, the Schmidt number, Sc to 0.25 and the Prandtl number, Pr to 0.7. The small discrepancy between the numerical and experimental results may be attributed to the inaccuracy of the correlation (e.g. r usually ranges between 0.33 and 0.4). In the absence of direct experi-

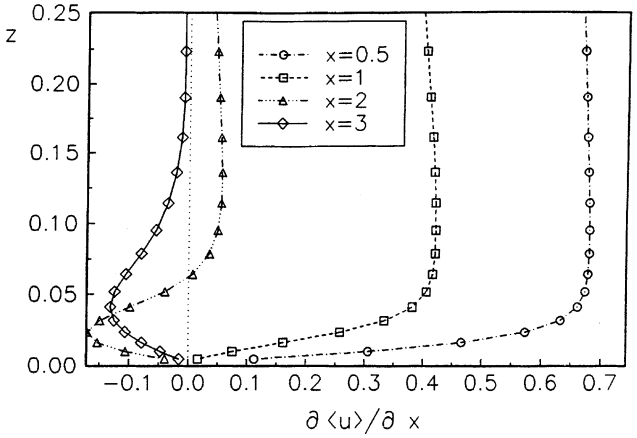

Fig. 7. Distribution of $\partial\langle u\rangle/\partial x$ along z ($0 \leqslant z \leqslant 0.25$) at different x locations, $Re_B = 5800$.

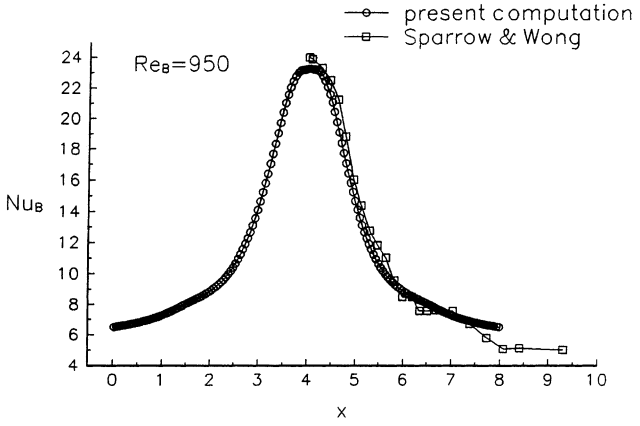

Fig. 8. Comparison of predicted Nusselt number with the experimental result of Sparrow and Wong (1975).

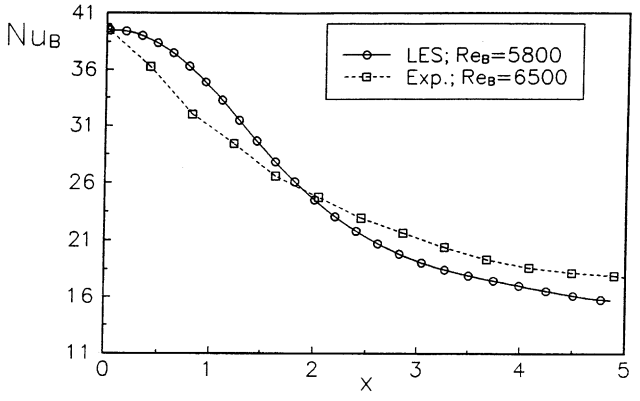

Fig. 9. Comparison of predicted Nusselt number with the experimental result of Schlünder et al. (1970).

mental measurements at $Re_B = 950$, we compared our numerical results with the measured values of Schlünder et al. (1970), who did experiments at a Reynolds number of 6500. The comparison of span-average Nusselt number distribution has been shown in Fig. 9. The comparison shows a reasonably good agreement, especially at the stagnation point. The numerical value of the Nusselt number at the stagnation point is 39.94, whereas Schlünder et al. (1970) predict the stagnation Nusselt number as 39.70.

4. Concluding remarks

Large eddy simulation has been used to simulate the low field of an impinging jet emanating from a rectangular slot nozzle. A localization procedure due to Piomelli and Liu (1995) has been used to implement the dynamic eddy viscosity. Exit boundary conditions have been used instead of the more usual periodic boundary conditions. The computed results show flow structures of the impinging jet. Distributions of the mean velocities, the turbulent stresses and the velocity fluctuations have been reported. The self-similar behavior of the axial velocity confirms the accuracy of the simulation. The predicted distribution of root-mean-square normal velocity is verified with the available experimental results. The model is able to predict subtle features of turbulence production rate. The negative production rate of turbulent kinetic energy takes place in the near wall region, close to the jet centerline. Finally, the computation has been extended to calculate the temperature field. The heat transfer results were compared with the experimental results of Sparrow and Wong (1975) and Schlünder et al. (1970). A good degree of accuracy has been observed in prediction of heat transfer at the stagnation zone.

Acknowledgements

The research has been funded by the Deutsche Forschungsgemeindschaft as a project of the Forschergruppe Wirbel And Wärmeübergang. Two of us (GB and HC) are grateful to the Alexander von Humboldt Stiftung and the German Academic Exchange Service, respectively, for the sponsorship. The authors are grateful to the unknown referees for the valuable comments. They record their acknowledgement for Prof. V. Eswaran of the Indian Institute of Technology Kanpur for useful suggestions.

References

Antonia, R.A., Browne, L.W.B., Rajagopalan, S., Chambers, A.J., 1983. On the organized motion of a turbulent plane jet. J. Fluid Mech. 134, 49–66.

Antonia, R.A., Chambers, A.J., Britz, D., Browne, L.W.B., 1986. Organized structures in a turbulent plane jet: topology and contribution to momentum and heat transport. J. Fluid Mech. 172, 211–229.

Baughn, J.W., Shimizu, S., 1989. Heat transfer measurements from a surface with uniform heat flux and impinging jet. J. Heat Transfer (ASME) 111, 1096–1098.

Becker, H.A., Massaro, T.A., 1968. Vortex evolution of a round jet. J. Fluid Mech. 31, 435–448.

Bradbury, L.J.S., 1965. The structure of a self-preserving turbulent plane jet. J. Fluid Mech. 23, 31–64.

Canuto, V.M., Cheng, Y., 1997. Determination of the Smagorinsky–Lilly constant C_S. Phys. Fluids 9, 1368–1378.

Childs, R.E., Nixon, D., 1986. Unsteady three-dimensional simulations of a VTOL upwash fountain. AIAA Paper, 86-0212.

Craft, T.J., Graham, L.J.W., Launder, B.E., 1993. Impinging jet studies for turbulence model assessment II. An examination of the performance of four turbulence models. Int. J. Heat Mass Transfer 36, 2685–2697.

Cziesla, T., Braun, H., Biswas, G., Mitra, N.K., 1996. Large-eddy simulation in a channel with exit boundary conditions. ICASE Report 198304, No. 96-18, NASA Langley Research Centre, USA.

Cziesla, T., 1998. Grostruktursimulation der Strömungs- und Temperaturfelder von Prallstrahlen aus Schlitzdüsen. Doctoral Disseratation, Ruhr Universitat Bochum, Reihe 19, Nr. 108, VDI Verlag, Dusseldorf, Germany.

Donaldson, C.B., Snedekar, R.S., Margolis, D.P., 1971. A study of free jet turbulent structure and impingement heat transfer. J. Fluid Mech. 45, 477–512.

Gao, S., Voke, P.R., 1995. Large-eddy simulation of turbulent heat transport in enclosed impinging jets. Int. J. Heat Fluid Flow 16, 349–356.

Germano, M., Piomelli, U., Moin, P., Cabot, W.H., 1991. A dynamic subgrid-scale eddy viscosity model. Phys. Fluids A 3, 1760–1765.

Gardon, R., Akfirat, J.C., 1965. The role of turbulence in determining the heat transfer characteristics of impinging jets. Int. J. Heat Mass Transfer 8, 1261–1272.

Ghosal, S., Lund, T.S., Moin, P., Akselvoll, K., 1995. A dynamic localization model for large eddy simulation of turbulent flows. J. Fluid Mech. 286, 229–256.

Ghosal, S., 1999. Mathematical and physical constraints on large-eddy simulation of turbulence. AIAA J. 37, 425–433.

Grinstein, F.F., Oran, E.S., Boris, J.P., 1987. Direct numerical simulation of axisymmetric jets. AIAA J. 25, 92–98.

Grötzbach, G., 1986. Direct numerical and large eddy simulation of turbulent channel flows. In: Cheremisinoff, N.P. (Ed.), Encyclopedia of Fluid Mechanics, vol. 6, Gulf Publishing Company, Texas, USA, pp. 1337–1391.

Gutmark, E.F., Wygnanski, I., 1976. The planar turbulent jet. J. Fluid Mech. 73, 465–495.

Gutmark, E., Wolfshtein, M., Wygnanski, I., 1978. The plane turbulent impinging jet. J. Fluid Mech. 88, 737–756.

Harlow, F.W., Welch, J.E., 1965. Numerical calculation of time dependent viscous incompressible flow of fluid with free surface. Phys. Fluids 8, 2182–2188.

Hoffmann, G., Benocci, C., 1994. Numerical simulation of spatially developing planar jets. AGARD-CP-551, pp. 26.1–26.6.

Kim, J., Moin, P., 1985. Application of a fractional-step method to incompressible Navier-Stokes equations. J. Comput. Phys. 59, 308–323.

Laschefski, H., Braess, D., Haneke, H., Mitra, N.K., 1994. Numerical investigation of radial jet reattachment flows. Int. J. Numer. Methods Fluids 18, 629–646.

Laschefski, H.T., Biswas, G., Mitra, N.K., 1996. Numerical investigation of heat transfer by rows of rectangular impinging jets. Numer. Heat Transfer A 30, 87–101.

Laschefski, H., Cziesla, T., Mitra, N.K., 1997. Evolution of flow structure in impinging three-dimensional axial radial jets. Int. Numer. Methods Fluids 25, 1083–1103.

Le, H., Moin, P., Kim, J., 1997. Direct numerical simulation of turbulent flow over a backward-facing step. J. Fluid Mech. 330, 349–374.

Leschziner M.A., Ince, N.Z., 1994. Computational modeling of three dimensional impinging jets with and without cross flow using second moment closure. UMIST Ref. TFD/94/06, Manchester, UK.

Lilly, D.K., 1967. The representation of small-scale turbulence in numerical simulation of experiments. In: Proceedings of the IBM Sci. Comp. Symposium on Environmental Scineces, Yorktown Heights, New York, pp. 195–210.

Lilly, D.K., 1992. A proposed modification of the Germano subgrid-scale closure method. Phys. Fluids A 4, 633–635.

Martin, H., 1977. Heat and mass transfer between impinging gas jets and solid surface. In: Hartnett, J.P., Irvine, T.F. (Eds.), Advances in Heat Transfer, vol. 13, pp. 1–60.

Mittal, R., Moin, P., 1997. Suitability of upwind-biased finite difference schemes for large-eddy simulation of turbulent flows. AIAA J. 35, 1415–1417.

Mumford, J.C., 1982. The structures of large eddies in fully developed turbulent shear flows. Part-1: the plane jet. J. Fluid Mech. 118, 241–268.

Najjar, F.M., Tafti, D.K., 1996. Study of discrete test filters and finite difference approximations for the dynamic subgrid-scale stress model. Phys. Fluids 8, 1076–1088.

Namer, I., Ötügen, M.V., 1988. Velocity measurements in a plane turbulent air jet at moderate Reynolds numbers. Exp. Fluids 6, 387–399.

Piomelli, U., 1994. High Reynolds number calculations using the dynamic subgrid-scale stress model. Phys. Fluids A 5, 1448–1490.

Piomelli, U., Liu, J., 1995. Large-eddy simulation of rotating channel flows using a localized dynamic model. Phys. Fluids 7, 839–848.

Schlünder, E.U., Krötzsch, P., nad Hennecke, F.W., 1970. Gesetzmäigkeiten der Wärme-und Stoffübertragung bei der Prallströmung aus Rund-und Schlitzdüsen. Chemie-Ing.-Techn. 42, 333–338.

Schumann, U., 1975. Subgrid scale model for finite difference simulations of turbulent flows in plane channels and annuli. J. Comput. Phys. 18, 376–404.

Smagorinski, J., 1963. General circulation experiments with primitive equations, I – the basic experiment. Monthly Weather Rev. 91, 99–164.

Sparrow, E.M., Wong, T.C., 1975. Impingement transfer coefficients due to initially laminar slot jets. Int. J. Heat Mass Transfer 18, 597–605.

Suga, K., 1995. Development and application of nonlinear eddy viscosity model sensitized to stress and strain invariants. Ph.D. Thesis, UMIST, Manchester, UK.

Viskanta, R., 1993. Heat transfer to impinging isothermal gas and flame jets. Expt. Thermal Fluid Sci. 6, 111–134.

Voke, P.R., Gao, S., 1998. Numerical study of heat transfer from an impinging jet. Int. J. Heat Mass Transfer 41, 671–680.

Zang, Y., Street, R.L., Koseff, J.R., 1993. A dynamic subgrid-scale model and its application to turbulent recirculating flows. Phys. Fluids A 5, 3186–3196.